Geochemistry, Geophysics, Geosystems

RESEARCH ARTICLE
10.1029/2018GC007765

Special Section:
FRONTIERS IN GEOSYSTEMS: Deep Earth - surface interactions

# Spatial Variations in Vent Chemistry at the Lucky Strike Hydrothermal Field, Mid-Atlantic Ridge (37°N): Updates for Subseafloor Flow Geometry From the Newly Discovered Capelinhos Vent

V. Chavagnac[1], T. Leleu[1], F. Fontaine[2,3], M. Cannat[2], G. Ceuleneer[1], and A. Castillo[1]

[1]Geosciences Environnement Toulouse, Université de Toulouse, Toulouse, France, [2]Institut de Physique du Globe de Paris, Paris, France, [3]Observatoire Volcanologique du Piton de la Fournaise, La Plaine des Cafres, Réunion, France

**Key Points:**
- Capelinhos is a new hydrothermal vent found at Lucky Strike hydrothermal vent
- We propose a new model of hydrothermal fluid circulation at Lucky Strike hydrothermal field
- Up to 65% of dissolved hydrothermal Fe is stored along the hydrothermal upflow zone

**Supporting Information:**
- Supporting Information S1

**Correspondence to:**
V. Chavagnac,
valerie.chavagnac@get.omp.eu

**Citation:**
Chavagnac, V., Leleu, T., Fontaine, F., Cannat, M., Ceuleneer, G., & Castillo, A. (2018). Spatial variations in vent chemistry at the Lucky Strike hydrothermal field, mid-Atlantic ridge (37°N): Updates for subseafloor flow geometry from the newly discovered Capelinhos vent. *Geochemistry, Geophysics, Geosystems*, *19*, 4444–4458. https://doi.org/10.1029/2018GC007765

Received 20 JUN 2018
Accepted 1 OCT 2018
Accepted article online 5 OCT 2018
Published online 12 NOV 2018



**Abstract** This study aims at characterizing the subseafloor architecture of the Lucky Strike hydrothermal field (LSHF) based on an extensive chemical database of the various vents. Our analysis is motivated by the discovery in 2013 of a new active high-temperature site, named Capelinhos, approximately 1.5 km east of the LSHF. Capelinhos fluids display particular chemical features with chloride and metal (Fe and Mn) concentrations 2 times lower and 4 times higher, respectively, compared to other vent sites. Trace element partitioning over the entire chlorinity range indicates a single deep fluid source feeding all the venting sites. Applying the Si-Cl geothermobarometer at Capelinhos, we find phase separation conditions at 435–440 °C and 370–390 bars (2,500–2,800 m below seafloor) consistent with former estimates for the LSHF, while temperatures of fluid-rock last equilibrium are estimated at ~400 °C for Capelinhos and 350–375 °C for the other sites based on the Fe-Mn geothermometer. We interpret these discrepancies in thermodynamic conditions beneath the sites in terms of crustal residence time, which are likely related to permeability variations across the hydrothermal upflow zone. We propose that conductive cooling of the upflowing fluids from the phase separation zone to the seafloor, beneath the main field vent sites, lowers the T conditions of last fluid-rock equilibrium, enabling ~65% of Fe mobilized in the reaction zone to be stored. In comparison, Capelinhos fluids are transported more rapidly from the reaction zone to the seafloor along a high-angle fracture system. The fluids venting at Capelinhos are more representative of the deeper part of the hydrothermal reaction zone.

## 1. Introduction

Hydrothermal fluid circulation at mid-ocean ridges is one of the major processes controlling the cooling of the oceanic lithosphere (Chen & Morgan, 1990; Stein & Stein, 1994), the geochemical composition of the crust (Alt, 1995; Alt & Teagle, 2003; Barker et al., 2008; Brant et al., 2012; Kelley & Delaney, 1987; Kelley & Robinson, 1990), the chemical composition of the ocean (Elderfield & Schultz, 1996; Resing et al., 2015), and the development of peculiar chemo-synthetic ecosystems (Martin et al., 2008, and references therein). Increasing attention has been drawn to the study of black smokers since their discovery along the East Pacific Rise off the Galapagos Islands in 1977. They have shown an unexpected diversity in geological setting, hydrothermal ecosystems, and fluid chemistry (Campbell et al., 1988; Douville et al., 2002; Ludwig et al., 2006; Schmidt et al., 2007, 2011; Von Damm, 1988, 2000). From the recharge zone to the discharge area, seawater is transformed into a high-temperature hydrothermal fluid, acquiring its chemical composition in a reaction zone, which is univocally pictured on top of axial magmatic chambers (AMC) at least along magmatically robust sections of fast (e.g., East Pacific Rise, 9°50′N), intermediate (e.g., Endeavour segment, Juan de Fuca Ridge), and slow spreading (e.g., Lucky Strike, 37°17′N) ridges. The chemical composition of high-temperature fluids can be further modified by either interaction with the rocks along the upflow pathway to the seafloor or precipitation of secondary minerals, depending on the fluid velocity (Coogan, 2008; Lowell, 2003; Saccocia & Seyfried, 1994; Steele-MacInnis et al., 2012). Thus, highlights that the *P-T* estimates for reaction zone conditions are sensitive to the geochemical tracer used and clear depth boundaries of the reaction zone cannot be easily drawn. The water-rock interactions that form hydrothermal fluid formation from seawater occur over a wide range of pressure and temperature conditions, that is, from the deepest part of the hydrothermal cell to the discharge at the seafloor, $\Delta P$ and $\Delta T$ can be a few hundred bars and degree Celsius, respectively. Chemical

variations can be identified depending on the nature of the substratum, that is, extrusive basaltic and/or mantellic substrate. The chemical compositions of focused hydrothermal fluids are used to constrain the range of pressure and temperature conditions at which water-rock interactions take place in the crust (Mottl et al., 2011; Reeves et al., 2011; Seyfried, 2003; Seyfried et al., 1998; Von Damm et al., 2003). The purpose of the present study is to gain insight on the subseafloor flow geometry using chemical analysis on fluids from different sites at the Lucky Strike hydrothermal field (LSHF).

LSHF was discovered at 37°N along the slow-spreading mid-Altantic ridge (MAR) in 1992 during the FAZAR cruise (Langmuir et al., 1997). The discovery motivated several subsequent research cruises with the objective of better characterizing the geological, geochemical, geophysical, and biological context of the vents (Barreyre et al., 2012; Charlou et al., 2000; Escartin et al., 2015; Fouquet et al., 1995; Langmuir et al., 1997; Ondréas et al., 2009; Pester et al., 2012; Von Damm et al., 1998). The first comprehensive study on the LSHF vent chemistry (Von Damm et al., 1998) indicated that the discharge of focused fluids (sampled in 1993 and 1996) originated from deep rooted fluids that underwent near-surface processes, for example, mixing with seawater, in the upflow zone (Von Damm et al., 1998). Charlou et al. (2000) analyzed fluids from 10 active sites of the LSHF. All samples were depleted in chloride relative to seawater (~420 to ~520 mM) with Cl increasing along a SE-NW transect across the LHSF. These authors proposed that a relatively shallow reaction zone provided vapor-like fluids (i.e., Cl below 545 mM of seawater) to the upflow zone at subcritical conditions (temperature and pressure lower than 407 °C and 298 bars respectively, equivalent to ~1,300 m below seafloor [mbsf]; Bischoff, 1991). Chemical data presented by Charlou et al. (2000) also suggested that vapor-dominated fluids underwent substantial subsurface mixing with altered seawater prior to venting as indicated by variable Sr isotope signatures with Cl concentrations still below that of seawater.

Eleven years later, Pester et al. (2012) used trace element and chloride covariation in fluids at five active vents to infer P-T equilibrium conditions during upflow. The samples display both chloride depletion and enrichment relative to seawater (from 414 to 588 mM). These authors proposed that (1) a unique and deep source feeds the hydrothermal field and (2) fluids underwent phase separation at 430–475 °C and 410–480 bars (~2,400–3,100 mbsf), that is, much higher P-T conditions than those proposed by Charlou et al. (2000). They attributed the variability observed in fluid chlorinity to subtle changes in pressure and/or temperature. These authors also argue that after phase separation and prior to discharge, the hot fluids cooled conductively and equilibrated with the greenschist facies of basaltic host rocks at lower temperatures (i.e., 350–380 °C).

These different models of the plumbing circulation system below the LSHF highlight the difficulties that arise when interpreting the chemical composition of vent fluids. This is compounded by the lack of contemporaneous observations between the studied sites. The EMSO-Azores program started in 2010 (FP6-ESONET; Person et al., 2009; Colaço et al., 2011) and led to the setup of a deep-sea observatory at LSHF. High-temperature hydrothermal fluids were collected yearly during maintenance cruises, which permitted the discovery of a new, high-temperature venting site, named Capelinhos ($T$ = 324 °C, Table 1) in 2013 (Escartin et al., 2015; Figure 1). Capelinhos lies approximately 1.5 km east of the LSHF and a few hundred meters from the seafloor emergence, one of the normal faults (referred as F2 in Combier et al., 2015) that rifts the Lucky Strike axial volcano. All other active/inactive venting sites are located to the west around a fossil lava lake on top of the volcano (Barreyre et al., 2012; Humphris et al., 2002; Ondréas et al., 2009, Figure 1).

In this study, we report on the first chemical data acquired for the Capelinhos vent site and we compare its chemical characteristics with those from 12 other active LSHF vents sampled during the same cruise in 2013. We use this data set to show that Capelinhos is a key site to assess the role of subsurface mixing, phase separation, and conductive cooling processes on the chemistry of the LSHF fluids and to propose an updated model of hydrothermal circulation below the field.

## 2. Geological Setting

The ~65-km-long Lucky Strike segment is located south of the Azores islands along the MAR between 37°03′N and 37°37′N (Detrick et al., 1995). The spreading rate is ~22 mm/yr (Cannat et al., 1999; Miranda et al., 2005). The LSHF is located on top of a volcano at the center of the segment. Seismic data have constrained the presence of an AMC at a depth of about 3,500 m below the summit of the volcano (Singh et al., 2006). Microseismic events recorded between 2007 and 2009 are located above the AMC at depths between

**Table 1**
*Summary of Fluid Sampling*

| Site | Depth (mbsl) | Longitude (W) | Latitude (N) | Hydrothermal group | pH[a] | Mg (mM)[b] | *n* sample | %SW[c] | T in situ (°C) |
|---|---|---|---|---|---|---|---|---|---|
| Capelinhos | 1665 | 32°15.830′ | 37°17.350′ | Capelinhos | 2.56 | 1.63 | 4 | 3.02 | 324 |
| Aisics | 1689.3 | 32°16.530′ | 37°17.338′ | south-east | 3.1 | 1.11 | 7 | 2.06 | 295 |
| Tour Eiffel | 1684 | 32°16.532′ | 37°17.343′ | south-east | 3.26 | 0.89 | 3 | 1.65 | 325 |
| Montségur | 1701 | 32°16.534′ | 37°17.284′ | south-east | 3.33 | 1.63 | 2 | 3.02 | 316 |
| Cyprès | 1738.7 | 32°16.863′ | 37°17.450′ | central | 2.84 | 1.53 | 3 | 2.84 | 304 |
| Isabel | 1683.7 | 32°16.638′ | 37°17.377′ | central | 2.93 | 1.55 | 3 | 2.87 | 224 |
| White Castle | 1708.9 | 32°16.869′ | 37°17.383′ | central | 2.9 | 1.18 | 3 | 2.18 | 317 |
| Crystal | 1723.3 | 32°16.921′ | 37°17.453′ | south-west | 3.17 | 1.61 | 2 | 2.98 | 335 |
| Sapins | 1718.6 | 32°16.888′ | 37°17.439′ | south-west | 3.56 | 3.6 | 3 | 6.67 | 280 |
| South Crystal | 1720.5 | 32°16.935′ | 37°17.445′ | south-west | 2.93 | 0.75 | 3 | 1.39 | 340 |
| Sintra | 1614.7 | 32°16.498′ | 32°17.529′ | north-east | 3.89 | 12.99 | 1 | 24.06 | 196 |
| Y3 | 1727.3 | 32°16.671′ | 37°17.512′ | north-east | 2.92 | 1.06 | 3 | 1.97 | 325 |

*Note*. The table presents location, depth, and details on fluid sampling for each site (minimum pH, minimum Mg measured and corresponding seawater entrainment, and maximum temperature measured in the vent prior to sampling).
[a]On board pH measurement at ambient temperature. [b]Minimum Mg measured on samples for each site. [c]Calculated from Mg concentration.

1,800 and 2,500 mbsf and interpreted as the product of active fracturing induced by penetration of colder down-flowing fluids into the hot rocks (Crawford et al., 2013). These microseismic events document the existence of two predominantly along-axis hydrothermal cells, with a central upflow zone centered beneath the LSHF. Seismic data suggest that the layer 2A depth is variable throughout the hydrothermal field (Arnulf et al., 2011).

The long known LSHF (Charlou et al., 2000, Chavagnac et al., 2018; Pester et al., 2012; Von Damm et al., 1998, Figure 1) comprises 20–30 sites with high-temperature black smokers ($T$ = 200–340 °C) and low-temperature diffuse venting (total area about 1,800 m$^2$, Barreyre et al., 2012). These sites are all clustered around a fossil lava lake (300 m in diameter; Fouquet et al., 1995) framed by two ancient volcanic cones, and one of which has been truncated by N010–N030° faults and fissures (Ondréas et al., 2009, Figure 1). The newly discovered

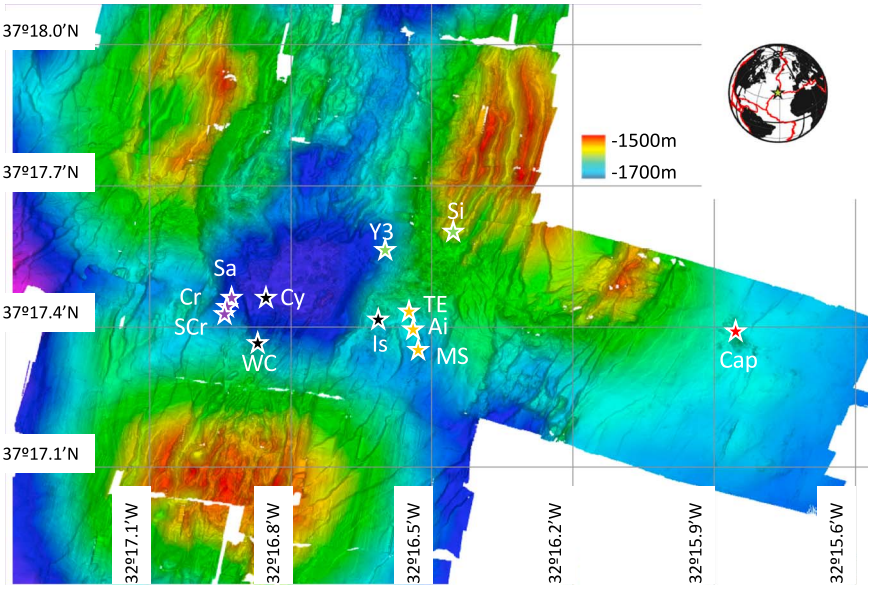


**Figure 1.** Bathymetric map of the Lucky Strike central volcano. Active hydrothermal vents are reported. Violet star: SW group composed of Sapins (Sa), Crystal (Cr) and South Crystal (SCr); yellow star: SE group composed of Tour Eiffel (TE), Aisics (Ai), and Montsegur (MS); green star: NE group composed of Sintra (Si) and Y3; black star: Central group composed of Cyprès (Cy), White Castle (WC), and Isabel (Is); the red star locates Capelinhos (Cap). See text for details. Microbathymetry from Ondréas et al. (2009). SW = south-west.

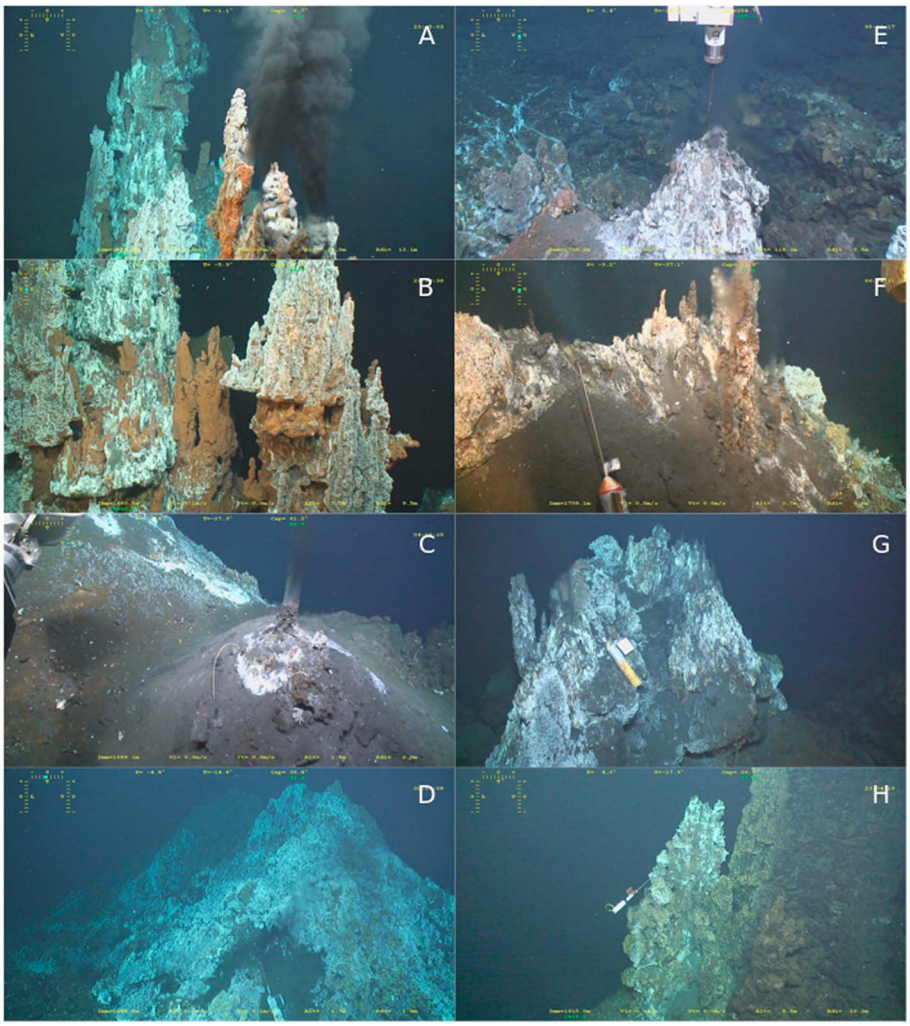


**Figure 2.** Overview of vent morphology. Snapshots of ROV videos (Ifremer-CNRS, MoMARsat 13), (a, b) Capelinhos; (c) Aisics; (d) Montsegur; (e) Cyprès; (f) White Castle; (g) Crystal; (h) Sintra. Figures 2a and 2b show candelabra-like structures that discharge focused high *T* fluid at Capelinhos vent site. Figures 12c and 12d show hydrothermal mounds in the southeastern hydrothermal area. The Aisics mound (Figure 2c) is not as developed as the Montsegur mound (Figure 2d) but both lack of tall indurated chimneys. Figures 2e–2g are situated in the southwestern hydrothermal area. There, high *T* vents are commonly set on elongated wall-like structures related to underlying fissures. Figure 2h is situated in the waning northeastern hydrothermal area and shows tall indurated chimneys, which are probably inherited from past intense activity. ROV = remotely operated vehicle; CNRS = Centre national de la recherche scientifique.

Capelinhos site is isolated and located 1.5 km to the east of the main field (Escartin et al., 2015). There, chimneys form *candelabra-like structure* on top of 10-m high sulfide mound and expel black smoker-type fluids at temperatures up to 324 °C (Figure 2 and Table 1). Diffuse venting is limited to the close vicinity of the black smokers, at the base of the edifice.

## 3. Sampling and Analytical Methods

### 3.1. Fluid Collection

The fluid samples studied in this paper were collected during the MoMARsat'13 EMSO-Azores maintenance cruise on the French Research vessel *Pourquoi Pas?* in September 2013. The 13 sampling sites (12 on LSHF and Capelinhos) were chosen to document the fluid diversity identified at LSHF by previous studies (Charlou et al., 2000; Chavagnac et al., 2015; Pester et al., 2012; Von Damm et al., 1998). Each vent site was sampled 4 times in succession (total duration of sampling $<$1 hr) to allow a better characterization of the

**Table 2**
*End-Member Composition of Fluids From the LSHF*

| Site | Group | Ca (mM) | K (mM) | Na (mM) | Fe (μM) | Mn (μM) | Si (mM) | Cl (mM) | $SO_4$ (mM) |
|---|---|---|---|---|---|---|---|---|---|
| Capelinhos | Cap | 17.97 ± 0.16 | 12.1 ± 0.3 | 205.0 ± 1.7 | 2789.4 ± 84.8 | 639.5 ± 27.6 | 14.1 ± 1.1 | 262.3 ± 0.1 | −0.4 ± 0.04 |
| Aisics | SE | 35.46 ± 1.44 | 19.6 ± 0.6 | 309.7 ± 19.7 | 417.6 ± 8.0 | 195.3 ± 4.0 | 14.86 ± 0.12 | 419.9 ± 1.8 | 0.11 ± 0.23 |
| Aisics | SE | 37.25 ± 0.12 | 19.0 ± 0.1 | 316.8 ± 1.1 | 452.03 ± 10.24 | 226.3 ± 4.86 | 15.7 ± 0.12 | 418.4 ± 1.1 | 0.02 ± 0.07 |
| Montségur | SE | 36.13 ± .46 | 19.6 ± 0.1 | 325.3 ± 0.8 | 283.7 ± 20.7 | 179.2 ± 8.4 | 15.25 ± 0.04 | 421.7 ± 1.3 | −0.06 ± 0.03 |
| Tour Eiffel | SE | 39 ± 0.64 | 19.7 ± 0.4 | 334.4 ± 6.5 | 574 ± 68.19 | 229 ± 15.51 | 15.1 ± 0.82 | 415.7 ± 4.7 | 0.9 ± 1.29 |
| Cyprès | Central | 43.24 ± 0.03 | 23.4 ± 0.1 | 399.3 ± 2.2 | 411.33 ± 16.64 | 309.01 ± 11.58 | 18.62 ± 0.27 | 519.7 ± 2.7 | −0.48 ± 0.08 |
| Isabel | Central | 39.6 ± 0.37 | 22.3 ± 0.2 | 373.8 ± 5.7 | 250.42 ± 21.29 | 147.05 ± 1.92 | 14.1 ± 0.3 | 470.3 ± 11.2 | −0.2 ± 0.31 |
| White Castle | Central | 38.35 ± 0.11 | 23.2 ± 0.1 | 381.8 ± 1.4 | 312.7 ± 11.37 | 254.44 ± 16.34 | 16.26 ± 0.11 | 481.4 ± 2.5 | −0.2 ± 0.01 |
| Crystal | SW | 53.55 ± 3.9 | 28.4 ± 0.1 | 445.9 ± 0.4 | 507 ± 68.55 | 260 ± 19.4 | 17,3 ± 0.77 | 569.5 ± 0.3 | 2.56 ± 2.69 |
| South Crystal | SW | 49.3 ± 0.8 | 28.3 ± 0.1 | 445 ± 1.5 | 593.4 ± 31.7 | 231.8 ± 10.04 | 17 ± 0.12 | 569.9 ± 1.3 | 0.1 ± 0.02 |
| Sapins | SW | 48.3 ± 0.72 | 26.6 ± 0.3 | 441.8 ± 4.7 | 201.7 ± 21.6 | 245.4 ± 14.45 | 17.5 ± 0.45 | 568.4 ± 8.8 | −0.28 ± 0.97 |
| Sintra | NE | 53.7 | 27.1 | 433.2 | 185.5 | 164.1 | 12.8 | 537 | 0.35 |
| Y3 | NE | 52.9 ± 0.5 | 25.5 ± 0.4 | 432.0 ± 4.5 | 686.7 ± 11.3 | 323.0 ± 18.0 | 17.1 ± 0.2 | 573.7 ± 8.5 | 0.03 ± 0.12 |
| Seawater | | 10.31 | 9.8 | 464 | 0 | 0 | 0.17 | 545 | 28.3 |

*Note*. The concentration of end-member fluids for each site is calculated based on linear least squares regression of element versus Mg, at Mg = 0 (Albarède et al., 1981; Ravizza et al., 2001; Figure S1.) n.d. = not determined; LSHF = Lucky Strike hydrothermal field.
[a]Temperature calculated by the Fe/Mn geothermometer and pressure estimated from Fe/Mn and Si concentrations (see text for details).

end-member hydrothermal fluid. In situ temperatures were measured in each vent prior to fluid sampling using the remotely operated vehicle (ROV) Victor 6000 high-temperature probe. High-temperature fluids were collected with 200 mL-titanium gas-tight samplers handled and triggered by the hydraulic arm of the ROV. The time between fluid samples at a given vent did not exceed 20 min. The samples were processed on board immediately after the ROV recovery. First, gases were extracted from the samplers and transferred into vacuumed stainless steel canisters or to ultraclean water sealed glass bottles, depending on the expected gas volume, for further analysis. The fluid samples were then extracted, filtered through 0.45-μm Millipore filters, and split into different aliquots for onshore analysis and stored at 4 °C. The pH, Eh, salinity, and conductivity were measured on board immediately after gas/fluid processing.

### 3.2. Analytical Methods

All the chemical analyses were conducted at the Geosciences Environment Toulouse laboratory. Ca, Na, K, Mg, Si, Fe, Mn, and Li concentrations were determined with an inductively coupled plasma atomic emission spectrometer Horiba Ultima2 instrument. Errors on analyses are indicated in Table 2. The instrument is calibrated using monoelemental solutions, multielemental solutions, and International Association for the Physical Sciences of the Oceans (IAPSO) standard solution (Besson et al., 2014). The latter is a seawater standard solution provided by OSIL and certified for its salinity. Salinity controls major element concentrations in seawater (Millero et al., 2008). Li concentration measurements of IAPSO give an average concentration of 24.6 ± 0.3 μM (rsd = 1%; $n$ = 4; 26.5 μM for seawater, Von Damm et al., 1998). The analytical drift is quantified by the standard bracketing after every eight samples. Analytical precision is better than 2%.

Sr, Rb, and Cs concentrations were measured using an inductively coupled plasma mass spectrometer Agilent500. The standard used was a NASS 6 solution (international seawater standard certified for some trace metals) and gives values of 79.1, 1.17, and 1.19 nM compared to 87, 1.4, and 2 nM of seawater values for Sr, Rb, and Cs, respectively ($n$ = 3). Drift corrections are made using an in-house multielementary standard doped with In and Re before analysis. Anions (Cl, $SO_4$, and Br) were determined by anionic chromatography calibrated with an IAPSO standard seawater solution.

Sr isotopic composition was measured at the Geosciences Environment Toulouse laboratory using a MAT FINIGAN 261 thermal ionization mass spectrometer. Analyses were performed on the samples that contain the lowest Mg concentrations. Sr was isolated from the matrix using Sr-Spec resin (Eichrom, USA). The $^{87}Sr/^{86}Sr$ ratio was defined as the average of 100 measurements of ion intensities following the static multicollection mode. The $^{87}Sr/^{86}Sr$ ratios were normalized to $^{86}Sr/^{88}Sr$ = 0.1194. Measured values for NBS 987 standard (recommended values of 0.710250) was $^{87}Sr/^{86}Sr$ = 0.710250 ± 0.000011 ($2\sigma_D$, $n$ = 14).

**Table 2** *(continued)*

| Site | Br (mM) | Rb (μM) | Sr (μM) | Li (μM) | Cs (μM) | 87Sr/86Sr | $T^a$ | $P^a$ |
|---|---|---|---|---|---|---|---|---|
| Capelinhos | 0.40 ± 0.02 | 18.7 ± 0.3 | 35.89 ± 0.65 | 197.3 ± 0.3 | 0.129 ± 0.003 | 0.70384 | 403 | 350 |
| Aisics | 0.65 ± 0.01 | 28.5 ± 0.1 | 80.06 ± 0.38 | 272.9 ± 0.3 | 0.184 ± 0.07 | 0.70422 | 368 | 225 |
| Aisics | 0.66 ± 0.04 | 28.5 ± 0.2 | 80.5 ± 0.7 | 266.3 ± 0.4 | 0.18 ± 0.001 | 0.70428 | 365 | n.d. |
| Montségur | 0.65 ± 0.02 | 28.3 ± 0.03 | 80.3 ± 1.1 | 265 ± 0.4 | 0.179 ± 0.002 | 0.70423 | 354 | 225 |
| Tour Eiffel | 0.64 ± 0.02 | 27.7 ± 1.3 | 81.16 ± 0.53 | 262.6 ± 0.4 | 0.179 ± 0.008 | 0.70448 | 376 | 300 |
| Cyprès | 0,84 ± 0.01 | 36.37 ± 0.47 | 112.47 ± 0.77 | 319 ± 0.3 | 0.222 ± 0.074 | 0.70403 | 345 | n.d. |
| Isabel | 0.73 ± 0.01 | 32.56 ± 1.39 | 105.0 ± 4.3 | 276.8 ± 04 | 0.199 ± 0.004 | 0.7043 | 357 | n.d. |
| White Castle | 0.75 ± 0.01 | 35.95 ± 0.1 | 111.19 ± 0.28 | 301.6 ± 0.1 | 0.221 ± 0.003 | 0.70502 | 341 | n.d. |
| Crystal | 0,88 ± 0.01 | 50 ± 5.65 | 180 ± 45.85 | 367.9 ± 0.3 | 0.231 ± 0.004 | 0.70414 | 364 | 300 |
| South Crystal | 0.89 ± 0.05 | 42.5 ± 0.11 | 125 ± 0.42 | 346.1 ± 0.4 | 0.260 ± 0.004 | 0.704 | 377 | 300 |
| Sapins | 0.87 ± 0.01 | 39.6 ± 0.87 | 118.1 ± 2.36 | 332.9 ± .5 | 0.243 ± 0.005 | 0.70429 | 322 | n.d. |
| Sintra | 0.85 | 39.3 | 115.5 | 343.5 | 0.244 | 0.70423 | 337 | n.d. |
| Y3 | 0.90 ± 0.01 | 42.3 ± 0.05 | 144.7 ± 0.6 | 323.3 ± 0.3 | 0.253 ± 0.001 | 0.70401 | 368 | 300 |
| Seawater | 0.84 | 2.0 | 87.0 | 25.6 | | 0.70916 | | |

We consider end-member hydrothermal fluids calculated by linear extrapolation to zero Mg of the least squares regression method (Table 2; Von Damm, 1988). The compositions of all analyzed samples for Sr isotope signature are given in the supporting information (Figure S1 and Table S1). For isotopic composition, the same method of linear extrapolation to a Mg/Sr equal to zero is used.

## 4. Results

### 4.1. Chloride, Sulfate, and Bromide

Hydrothermal fluids of the LSHF exhibit chloride concentrations between 415 mM for the south-east (SE) sites (Montsegur, Aisics, and Tour Eiffel; Figure 1) and 574 mM for the north-east (NE) sites (Y3 and Sintra) and the south-west (SW) sites (South Crystal, Crystal, and Sapins). White Castle, Isabel, and Cyprès sites have Cl concentration closer to seawater one at values ranging between 470 and 520 mM, also in line with previous data. Interestingly, Capelinhos has the lowest chloride concentration ever measured at LSHF at 262 mM (Table 2).

All fluids have $SO_4$ values close to zero. However, some of them (Crystal and Tour Eiffel) have calculated end-member value slightly higher than 0 probably due to anhydrite entrainment and dissolution (Von Damm et al., 1998; Table 2). Br concentrations have variations similar to Cl concentrations, whereby maximum Br concentrations are found in Y3 fluids at 0.88 mM close to the seawater value of 0.84 mM while minimum values are found for Capelinhos fluids at 0.38 mM.

### 4.2. Iron and Manganese

Capelinhos end-member fluid shows very high Fe and Mn concentrations of 2,789 and 639 μM, respectively. In comparison, Fe and Mn concentrations of LSHF end-member fluids vary between 155 (Sintra) and 593 μM (South Crystal) for Fe (Figure 3a) and between 164 (Sintra) and 232 μM (South Crystal) for Mn (Figure 3b).

### 4.3. Silica

Silica concentrations of hydrothermal end-members vary from 12.8 at Sintra (NE group) to 18.6 mM at Cyprès (SW group). The Si concentration at Capelinhos is 14.1 mM, a value similar to the one for the SE sites, despite distinct chlorinities (Figure 3c).

### 4.4. Sodium, Calcium, and Potassium

Na, Ca, and K constitute the major cations in the end-member fluids and are closely linked to Cl concentration due to charge balance. Maximum Na concentrations (445 mM) are found in Crystal and South Crystal fluids, while the minimum Na concentration (205 mM) is obtained for Capelinhos.

Maximum Ca concentration are found in Sintra, Y3, Crystal, and South Crystal fluids with values around 53 mM, while at Capelinhos the Ca concentration is the lowest one at 18 mM.

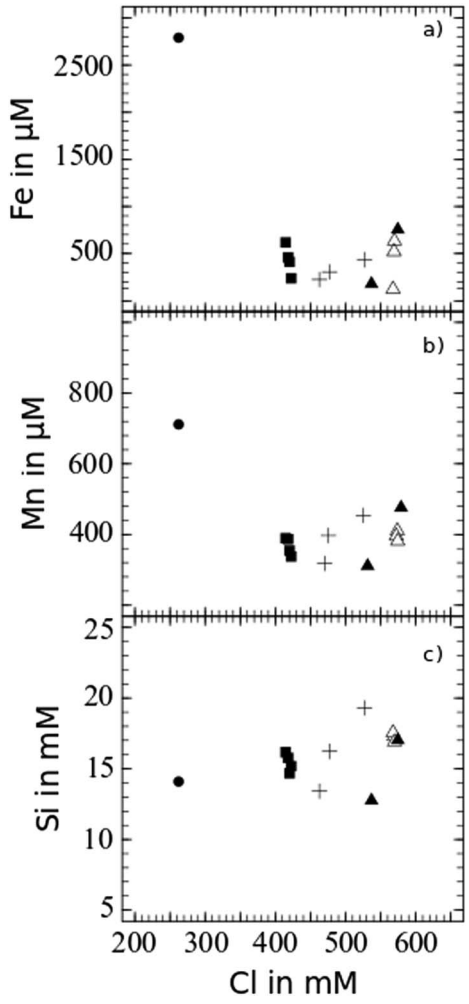


**Figure 3.** Fe, Mn, and Si versus Cl in end-member fluids (a) Fe versus Cl; (b) Mn versus Cl and (c) Si versus Cl. These diagrams show the lack of correlation of these elements relative to Cl.

Maximum K concentrations (28.3 mM) are found in South Crystal and Crystal, and the minimum concentration (12.1 mM) is measured at Capelinhos.

### 4.5. Rubidium, Strontium, Cesium, and Lithium

Rb, Cs, and Li are 10 to 20 times more enriched in the LSHF fluids compared to seawater, while Sr concentrations fluctuate around the seawater value at ±20%. Concentrations in Rb, Li, Cs, and Sr are correlated to the fluid chlorinity (Table 2). Minimum and maximum Rb concentrations are 18.7 and 50 µM for Capelinhos and Crystal, respectively. Minimum and maximum Li concentrations are 197.1 and 367.9 µM, also for Capelinhos and Crystal, respectively. Sr follows the same pattern with a maximum concentration of 180 µM for Crystal and a minimum concentration of 35.9 µM at Capelinhos.

### 4.6. Sr Isotopes

The least radiogenic end-member fluid compositions ($^{87}Sr/^{86}Sr = 0.70384$; Table 2) are obtained for Capelinhos. Y3, Crystal, and South Crystal on the northern and western side of the fossil lava lake have unradiogenic $^{87}Sr/^{86}Sr$ ratios ranging between 0.7039 and 0.7040. $^{87}Sr/^{86}Sr$ signatures of the Aisics, Tour Eiffel, and Montsegur sites are the most radiogenic ones at 0.7042–0.7043 (Table 2). The central sites display variable Sr isotope signatures, that is, Cyprès at 0.70403 and White Castle at 0.70502.

## 5. Discussion

### 5.1. Source(s) of Hydrothermal Fluids

Cl is the major anion present in hydrothermal fluids and controls the cation abundances due to the charge balance of the solution. We propose to define groups of sites based on Cl concentrations and spatial distribution on the seafloor. With the lowest salinity, Capelinhos (Cl = 262 mM) defines its own group; the SE group of sites is composed of Tour Eiffel, Montsegur, and Aisics with a $Cl_{average}$ of ~420 mM; the central group characterized by $Cl_{average}$ ~495 mM, comprises Isabel, White Castle, and Cyprès. We define SW and NE groups for which salinity values are all close to or above seawater, that is, SW group (Crystal, South Crystal, and Sapin sites; $Cl_{average}$: ~580 mM) and NE group (Y3 and Sintra sites; $Cl_{average}$: 574 and 537 mM). Due to the conservative behavior of Cl in hydrothermal system, this chemical tracer has been widely used to infer the *P-T* conditions of the phase separation zone. Charlou et al. (2000) proposed that Cl variability observed at the LSHF could be due to subcritical vapors mixing with altered seawater in subsurface conditions prior to fluid venting. To address this hypothesis, we use the Sr isotope compositions of the lowest Mg-rich hydrothermal fluids as a tracer of sources and mixing.

A hydrothermal fluid acquires its Sr isotopic signature from the rocks with which it interacts (Albarède et al., 1981), that is, basalt at LSHF. The contrasting Sr isotope compositions of basalt at 0.70298 and seawater at 0.70916 are favorable to the detection of any input of modified seawater in hydrothermal fluids. Any Sr isotopic signature of hydrothermal fluid end-member that departs from that of the basalt will suggest the contribution from an additional source (Berndt et al., 1988; Palmer, 1992; Ravizza et al., 2001). The most vapor-dominated fluid at Capelinhos exhibits the least radiogenic Sr isotopic composition at 0.70384. In comparison, the SE, NE, and SW groups that exhibit Cl concentrations at 420, 574, and 570 mM, respectively, display similar Sr isotopic signatures at 0.7042–0.7044 for SE sites and 0.7040 and 0.7042 for NE and SW sites (Table 2). In contrast, the central group (~495 mM of Cl) displays a wide range of $^{87}Sr/^{86}Sr$ ratios, ranging from 0.70403 to 0.70502. The observed range of $^{87}Sr/^{86}Sr$ ratios of fluid end-members does not correspond to the geographical distribution of sites around the fossil lava lake. Moreover, the $^{87}Sr/^{86}Sr$ ratios and the Cl contents of hydrothermal end-members do not correlate positively and linearly. In addition, it is unlikely that the

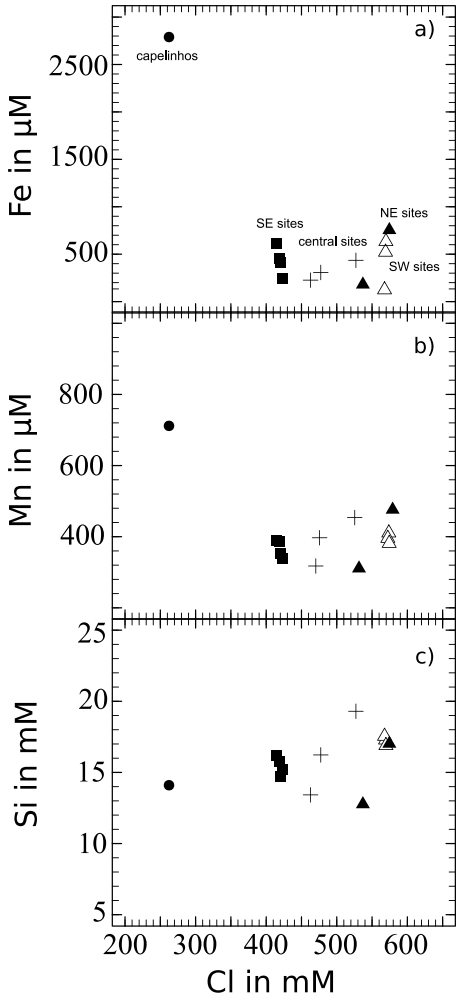


**Figure 4.** Log (Elt/Cl) versus log (Cl) diagram. Diagram of elt/Cl versus Cl showing the linear relationship between trace element and chlorinity, a proxy for the effect of phase separation.

variability of $^{87}Sr/^{86}Sr$ ratios is related to local differences in the substratum, as basalts from a wide selection of samples (including T- and mid ocean ridge basalt [MORB]) across the Lucky Strike segment have a well-constrained Sr isotopic signature of 0.70298 ± 0.00007 ($n$ = 13; Hamelin et al., 2013). The tight but significant differences in Sr isotopic signature between the highest and lowest chlorinity fluids mean that Capelinhos fluid, compared to the other sites, has less interaction with radiogenic Sr-rich material such as extensively altered rocks. The fact that $^{87}Sr/^{86}Sr$ is not correlated with Cl rules out a modified seawater component that would mix with hydrothermal fluid in subsurface. However, this does not rule out the contribution of a second deep-rooted hydrothermal cell to produce the Capelinhos fluid.

We investigate the distribution of trace element concentrations (Br, Li, Sr, Rb, and Cs) over the LSHF chlorinity range, following the methodology of Pester et al. (2012) to detect the potential occurrence of a second hydrothermal source. The elements considered are controlled by vapor/brine partition coefficients during phase separation (Berndt & Seyfried, 1990; Foustoukos & Seyfried, 2007a, 2007b; Foustoukos et al., 2004; Pester et al., 2015, among others). Li and Cs distributions exhibit a negative linear trend, while Rb and Sr show a positive trend, indicating a preferential partitioning to the vapor and brine phases, respectively (Figure 4). This is in line with previous studies (Berndt & Seyfried, 1990; Foustoukos & Seyfried, 2007a; Pester et al., 2015; Pokrovski et al., 2005). This is also coherent with the LSHF study of Pester et al. (2012), apart for Rb that shows less brine affinity with the extended Cl range of the present data set. Note, however, that without Capelinhos fluid, Rb presents a steeper linear slope at +0.38, identical to the one at +0.35 reported in Pester et al. (2012). Element vapor/brine partitioning can be summarized as follows: Sr $<$ Rb $<<$ Br $<<$Cs $<$ Li with increasing affinities for the vapor phase. Therefore, the linear correlation of each of these elements over the Cl range (from 262 to 574 mM; Figure 4) supports a phase separation process controlling overall trace element abundances, that is, a unique deep-rooted fluid source as proposed by Pester et al. (2012). This implies that being 1.5 km away from the other sites, Capelinhos is nevertheless fed by the same upflow zone and is part of the same hydrothermal cell.

### 5.2. Chlorinity Variability and Geographical Repartition

While the distribution of trace element suggests a unique source feeding the hydrothermal upflow at LSHF, the end-member fluids nevertheless display a wide range of chlorinity, from the most vapor-like, low-Cl fluids at Capelinhos to the brine-like, high-Cl fluids at Y3. Venting of low-Cl fluids can unambiguously be ascribed to phase separation processes at depth and flushing of buoyant vapor phase on the seafloor. However, the physics controlling the venting of brine-like fluids is more complex as their thermodynamical (viscosity and density) and surface properties (surface tension) counteract their buoyancy, impacting therefore their rise toward seafloor. In the literature, numerical models of two-phase flow including transport of salt (considered as NaCl) have proposed scenarios for brine venting (Coumou et al., 2009; Fontaine et al., 2007).

Phase separation leads to vapor and brine formation, but due to different physical behavior, that is, the wetting effect of the liquid/brine phase, brines will segregate and be stored in backwater porosity or will coat the walls of larger channels (Fontaine & Wilcock, 2006). As long as brine saturation is lower than a threshold value, the brines do not form a continuous medium and remain immobile. However, when this threshold is reached, and provided that the vertical pressure gradients in the upflow are high enough compared to brine density (if not, the brine is too dense and will sink down; Fontaine & Wilcock, 2006; Fontaine et al., 2007), then the brine phase is able to move upward. Fontaine and Wilcock (2006) showed that brine ($<$20–25 wt % NaCl) produced under supercritical conditions and stored within the rock

backwater porosity in the reaction zone could still flow toward the surface. Meanwhile, vapor phases flow preferentially through wider cracks (Fontaine & Wilcock, 2006; Goldfarb & Delaney, 1988) and are flushed to the seafloor. Fontaine et al. (2007) also developed the hypothesis that vertical permeability gradients could act as a barrier for brine upflow and tend to concentrate brine at the base of layer 2A. When the backwater porosity is saturated with brine, or during cooling of the system, brine can be entrained, and mixed with vapor or seawater salinity hydrothermal fluid, which leads to fluid discharge with higher salinity than seawater.

Alternatively, Coumou et al. (2009) conducted numerical modeling without a permeability gradient to investigate salinity variations at discharge zones for different bottom heat fluxes and system pressures. For a pressure of 150 bars at the seafloor and ~250 bars at the bottom of the system, that is, phase separation zone ~1,000 mbsf, the simulations show temporal variations in vent fluid salinity with several spikes at salinity higher than seawater over periods of several years. These salinity spikes are also associated with temperature spikes of a few degrees (<10 °C). Coumou et al. (2009) explained these salinity pulses as due to brine mobilization occurring when the porosity of the upflow zone becomes saturated. Further mixing of this brine with vapor-dominated fluids during the upflow produces a transient spike in salinity. Salinity then returns to the initial vapor-like one, while the brine layer builds up again and reduces saturation of the backwater porosity. In summary, modeling studies infer that sustained phase separation processes can drive brines to *oversaturate* the porous network causing their remobilization and flushing to the seafloor without major changes in the thermodynamic state of the hydrothermal cell.

Brine remobilization and flushing have been already observed and invoked in the natural hydrothermal environment, to explain Cl variability related to periodic (tides) brine flushing at the Main Endeavour Field (Larson et al., 2009). At LSHF, Y3 site exhibits Cl concentrations that increase from vapor-like values at 436 mM in 1993 (Von Damm et al., 1998) to brine-like ones at 574 mM in 2013 (this study, Table 2). We infer that this shift in fluid chlorinity of Y3 site could be ascribed to brine oversaturation and mobilization in the porous/fractured crust along the upflow zone, as venting temperature and reaction zone *P-T* conditions according to the geothermobarometers did not fluctuate significantly over that time period (Pester et al., 2011). Based on a study of tidal forcing on LSHF vent fluid temperatures, Barreyre and Sohn (2016) proposed that the permeability structure beneath the LSHF vents is variable, possibly reflecting variations of layer 2A thickness from 300 to 600 mbsf between the west and east of the fossil lava lake area. Such local variations would also be expected to impact brine storage and remobilization beneath the field. Finally, the yearly monitoring of the Y3 vent in comparison to other LSHF sites should provide key information of the temporal evolution of brine venting. Such information is particularly important to better design numerical models of hydrothermal flow dynamics and to gain more insight into the interrelationships among phase separation, brine storage, remobilization, and fate beneath the field.

### 5.3. Pressure and Temperature Conditions in the LSHF Hydrothermal System

#### 5.3.1. Conditions at the Base of Upflow Zone

Si and Cl end-member fluid concentrations have been used as a geothermobarometer to determine the depth of the top of the two-phase zone in several hydrothermal systems worldwide (Fontaine et al., 2009). This depth is considered a good estimate of the base of the upflow zone as phase separation induces large variations in the fluid flexibility (a measure of the ability of buoyancy-driven water to transport energy), providing the necessary buoyancy for the hydrothermal vapors to flow upward (Coumou et al., 2009; Jupp & Schultz, 2000). Cl concentration only changes in the two-phase zone, as soon as the vapor-dominated fluid starts to rise it returns to a single phase, and its Cl content is fixed for the remainder of the ascent to the seafloor, provided no mixing with seawater occurs. The Cl content of flushed vapors are thus representative of the conditions at the top of the two-phase zone. Using Cl-P-T solubility relationships (e.g., Driesner, 2007), one can estimate a range of possible conditions (an iso-Cl line) in *P-T* space for a given Cl. Now, considering that Si is in equilibrium with quartz during upflow/cooling and using Si-Cl-T-P solubility relationships (e.g., Foustoukos & Seyfried, 2007b), one can use the Cl and Si contents of the vented vapors to estimate another range (an iso-Si line) of possible *T-P* for a given Si. Intersection between these iso-Cl and iso-Si lines gives a unique *P-T* condition for the roof of the two-phase area. When applying the Si-Cl geothermobarometer to the Capelinhos fluids, we obtain a temperature of 438 °C and a pressure of 375 bars for the phase separation zone/base of the reaction zone, which corresponds to a depth of

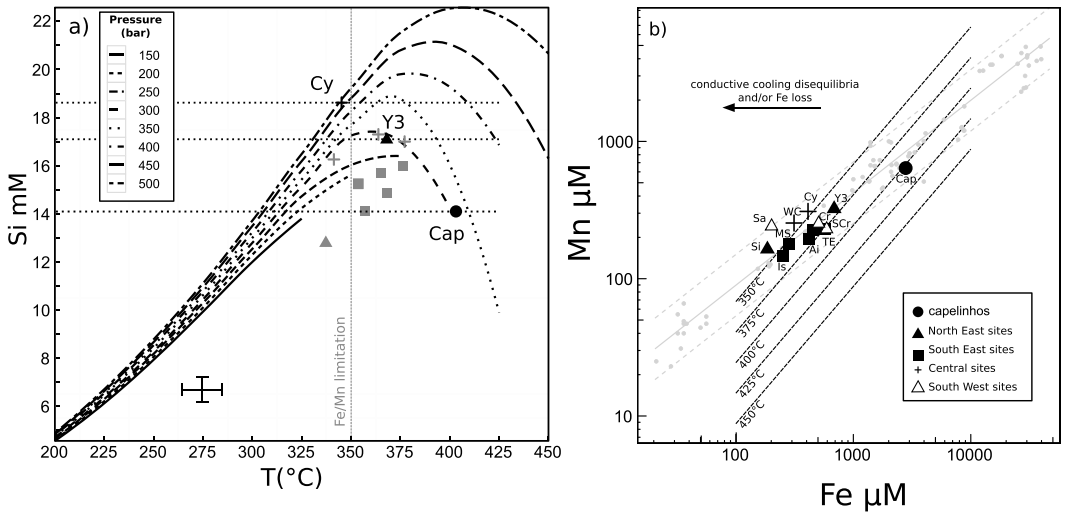


**Figure 5.** Geochemical information for *P* and *T*. (a) Quartz geothermobarometer based on Foustoukos and Seyfried (2007b). Points represent Si measured in fluids with calculated temperature based on the Fe-Mn geothermometer. Gray dashed lines represent the *classical* approach to evaluate *P* and *T* (see text for details). (b) Fe and Mn concentrations on a logarithm scale (modified from Pester et al., 2011). Gray line represents basalt alteration line, and black dashed lines are isotherms calculated from the Fe/Mn geothermometer.

2,600 mbsf (using a cold hydrostatic pressure gradient of $\rho$ = 800 kg/m$^3$, Fontaine et al., 2009). Using the Tour Eiffel chemical data for fluids collected in 1993 (Charlou et al., 2000), Fontaine et al. (2009) determined similar *P* and *T* conditions at 390 bars and 440 °C for the LSHF phase separation zone. Thus, the deepest part of the upflow zone is quite well constrained with similar estimates for fluids collected 20 years apart and at different site within the LSHF.

One should, however, be careful using this geothermobarometer as quartz may precipitate during upflow. Quartz veins in the ocean crust are often associated to greenschist facies minerals such as pyrite, chlorite, amphibole, and epidosite at different depth levels (Alt et al., 2010; Delaney et al., 1987; Heft et al., 2008; Honnorez, 2003). The vented Si concentration should, therefore, be taken as a minimum value (the actual Si content of the rising vapor being higher and not constrained) giving a minimum depth to the base of the upflow/roof of the two-phase area. The Si-Cl geothermobarometer developed by Fontaine et al. (2009) predicts that the estimated depth of the top of the two-phase zone would deepen by 70–100 m/mmol of Si at constant Cl. We note that the equilibrium pressure ranges of 375–390 bars derived with Si-Cl, that is, 2,600–2,800 msbf is in good agreement with the 2,300–2,900 mbsf maximum depth range for microseismic activity beneath the hydrothermal field (Crawford et al., 2013).

### 5.3.2. Conditions of Last Equilibrium in the Reaction Zone

Vent fluid Fe and Mn contents can be used to estimate the temperature of the fluid last equilibrium with greenschist facies rocks (Pester et al., 2011). For Capelinhos end-member fluids, which exhibit the highest Fe and Mn concentrations of all the LSHF fluids—equivalent to Fe concentration found at the Broken Spur (29°N) and Snake Pit (23°N) fields on the MAR (Campbell et al., 1988; James et al., 1995; Figure 5)—we find a minimum temperature of greenschist facies equilibrium at 403 °C. The Fe-Mn geothermometer does not provide means to calculate a corresponding equilibrium pressure. If we assume that both quartz and fluid-greenschist (Fe and Mn bearing) minerals facies reached equilibrium concomitantly, that is, that the Capelinhos fluids interacted minimally with the surrounding rocks during their ascent from the phase separation zone, then the equilibrium temperature is obtained from the Fe-Mn geothermometer and the vent fluid Si concentration permits to calculate a corresponding equilibrium pressure using Cl-T-P-dependent solubility relationships (Foustoukos & Seyfried, 2007b; Von Damm et al., 1991). At Capelinhos (Si = 14.1 mM, Cl = 260 mM), the estimated equilibrium pressure is 350 bars, that is, a depth of ~2,300 mbsf (Figure 5a). Applying the same approach to the most brine-dominated hydrothermal fluids from the other LSHF sites, that is, the SW group and Y3 of the NE group, indicates a lower pressure (300 bars, i.e., ~1,600 mbsf) and cooler temperatures 350–375 °C for the last fluid-rock equilibrium. These differences in *P-T* conditions of

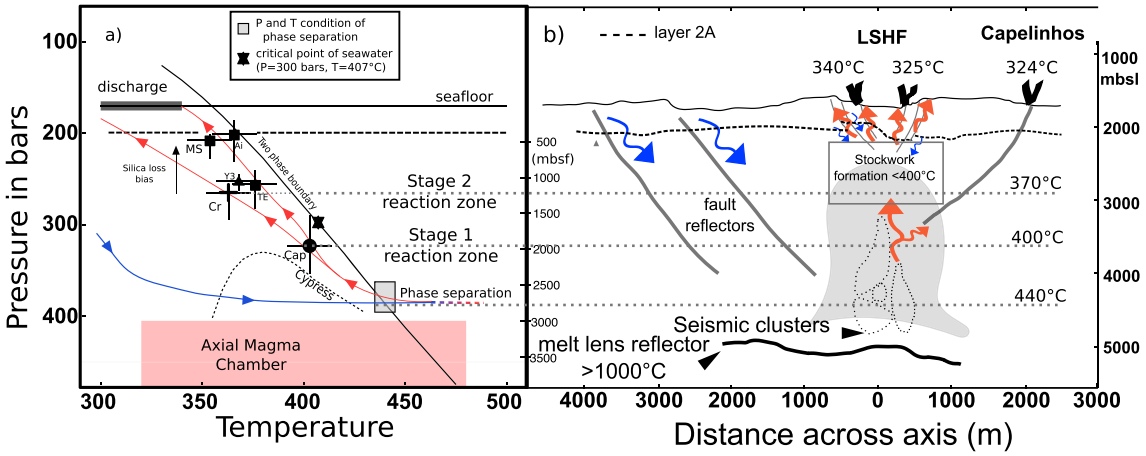


**Figure 6.** Fluid circulation. (a) Calculated *P* and *T* of some vents at equilibria with quartz are presented. *P* and *T* were calculated using the Fe/Mn geothermometer of Pester et al. (2011), quartz geothermobarometer (Foustoukos & Seyfried, 2007b), and NaCl-$H_2O$ solution properties (Driesner & Heinrich, 2007, see details in text). Dotted lines represent the depth of the base of layer 2A for western and eastern sites (Arnulf et al., 2011). The red shaded domain represents the range of depth to the top of the axial magma chamber as identified by Singh et al. (2006) and Combier et al. (2015). Gray lines represent fault labeled F1 and F1b in Combier et al. (2015); dotted gray line correspond to F2. The blue line represents the inferred *P-T* path in the recharge zone where cold seawater percolates through oceanic crusts and gradually interacts with rocks. Red lines represent the inferred *P-T* path in the upflow zone, based on the conditions estimated from fluid chemistry. The gray rectangle represents the phase separation zone estimated from the Si and Cl concentrations in the low salinity fluids (Capelinhos, TE) using the geothermobarometer proposed by Fontaine et al. (2009). (b) Modified from Escartin et al. (2015). Cartoon representing the hydrothermal cell under the LSHF. Blue arrows represent downward flow of seawater; red arrows are focused hot fluid moving upward through cracks and faults. Seismic clusters are from Crawford et al. (2013). F1, F1b, and F2 are from Combier et al. (2015). LSHF = Lucky Strike hydrothermal field.

last fluid-rock equilibrium between the Capelinhos and the other LSHF sites probably indicate that the fluids venting at Capelinhos ascend more rapidly from the phase separation zone than the fluids venting at the other sites so that they react less with the lost rocks upon ascent. This interpretation is also consistent with the least radiogenic Sr isotope signature of Capelinhos end-member fluids that we interpret as the most representative of the basaltic substratum (section 5.1). We thus propose that the observed variability in fluid composition between the LSHF vent sites primarily results from variable fluid residence times within the different areas that compose the upflow zone. We discuss a possible geological factor controlling these processes at Lucky Strike in the next section.

### 5.4. Fluid Circulation Pathway at LSHF

Based on the Si-Cl geothermobarometer that is in agreement with the depth of microseismic activity (Crawford et al., 2013), we propose that fluids at Lucky Strike start to upflow from a depth/pressure of 2,600–2,800 mbsf/370–390 bars at 430–440 °C below the lava lake. Capelinhos is located 300 m to the east of a west dipping fault that has been imaged in seismic reflection data and shown to extend at least down to a few hundred meters below seafloor under the volcano (F2 in Combier et al., 2015, Figure 6). We infer that small offset faults and fractures parallel to this fault and belonging to the same network may intersect the seafloor near Capelinhos (Escartin et al., 2015). We propose that this fault and fracture network intercepts the hydrothermal upflow zone at depth, in the intrusive section (layer 2B), creating a fast-extraction pathway for hydrothermal fluids venting at Capelinhos because of enhanced hydraulic properties (e.g., permeability and porosity) due to tectonically produced faults and fissures (Caine et al., 2010, Figure 6). This *transverse* and longer (compared to a vertical flow) flow path leads to significant cooling from 403 °C in the phase separation zone to 324 °C at the vent field, but the fast fluid migration and short residence time prevent extensive fluid-rock reactions, and the exiting fluids preserve their metal content. On the other hand, the fluids exiting at the main LSHF sites distributed around the lava lake would rise almost vertically but more slowly due to the lower overall permeability of younger intrusives beneath the fossil lava lake (Arnulf et al., 2011). This longer residence time allows fluids to interact more extensively with the crust to temperature down to 350 °C, and to precipitate a large part of their metal content, as secondary greenschist minerals including Fe-bearing phases like chlorite.

The low Fe-Mn ratios of the main LSHF sites (~0.8 to 2.5), compared to Capelinhos fluids at ~4.4 (Figure 4), reflects a significant Fe loss within the upflow zone. By using Capelinhos fluids as a reference, we calculate

that ~65% (±14%) of dissolved hydrothermal Fe from sites located around the fossil lava lake is stored most likely as secondary minerals between the phase separation zone and the seafloor. In other words, only ~35% of Fe mobilized in the reaction zone is discharged as dissolved phase into the deep seawater mass at the LSHF.

## 6. Conclusion

In 2013, a new active site, named Capelinhos, was discovered at LSHF approximately 1.5 km east of the main Lucky Strike axial graben and fossil lava lake, where the well-known LSHF vents are located. Capelinhos vents high-temperature black smoker fluids at 324 °C. Its fluid chemistry has two distinct characteristics compared to the other LSHF vent sites: (1) the lowest Cl concentration at ~260 mM ever measured at LSHF and (2) the highest Fe and Mn concentration (2,800 and 640 μM respectively). The discovery of this site provides the opportunity to reassess the thermodynamic condition within the reaction zone. Applying the Si-Cl geothermobarometer of Fontaine et al. (2009), we show that Capelinhos fluids were formed at supercritical conditions, as well as the other vapor-dominated fluids from LSHF. The temperature of the phase separation zone is 438 °C at 2,600 mbsf. These results are in agreement with the maximum depth of microseismic events reported in Crawford et al. (2013), which are interpreted as due to rapid heat exchange between hot rocks and downgoing hydrothermal fluids.

Applying other geochemical indicator, such as Fe-Mn geothermometer of Pester et al. (2011), a range between ~370 °C for LSHF fluids and ~400 °C for Capelinhos is obtained. By combining quartz solubility with these calculated temperatures, the minimum equilibration temperature and pressure in the reaction zone appears to be deeper for Capelinhos fluids (350 bars) than for LSHF (300 bars). Because the fluids vent at temperatures that are still well within the greenschist facies realm, these conditions are not considered as completely representative of the top of the reaction zone. More accurately, they are indicative of significant differences in the residence time of the fluid in the upflow zone between Capelinhos and the other LSHF vents.

We propose a revised model of the hydrothermal path based on the discovery of Capelinhos. When crossing the two-phase boundary, at ~2,600 mbsf, the fluid starts flowing upward, with brine entrainment to different extent from site to site. At the fossil lava lake, fluids (vapor and brines) undergo more conductive cooling than Capelinhos vent along their upflow to the surface due to longer residence time in the substratum. Brine mixing and cooling processes likely result in the formation of secondary Fe-bearing minerals like chlorite beneath the fossil lava lake, resulting in the storing of up to 65% of Fe mobilized in the reaction zone. Fluids discharging at Capelinhos (the most vapor-dominated fluid of the LSHF) reach the sea surface by a high angle normal fault zone and undergo significant cooling but still preserve high dissolved Fe and Mn concentrations.

**Acknowledgments**

We thank the *Pourquoi Pas?* and Genavir crew as well as the ROV team for their tremendous work during the cruise. We are grateful to the chemistry facility of the Géoscience Environment Toulouse laboratory (GET). Supporting information provides geochemical and Sr isotope signature of hydrothermal fluids. All geochemical measurements made aboard are available in the cruise report at the following doi: https://doi.org/10.17600/13030040. Leleu acknowledges the French Ministry of Education and Research for the financial support of his Ph.D. fellowship. We also acknowledge financial support from the French ANR Lucky Scales Project (ANR-14-CE02-0008-03) and the EU project EMSO (http://www.emso-eu.org/). We are also grateful for the suggestions and constructive comments of N. Pester, W. Wilcock, J.A. Resing, and two anonymous reviewers on different versions of this manuscript.

## References

Albarède, F., Michard, A., Minster, J.-F., & Michard, G. (1981). $^{87}Sr/^{86}Sr$ ratios in hydrothermal waters and deposits from the East Pacific Rise at 21°N. *Earth and Planetary Science Letters*, *55*(2), 229–236. https://doi.org/10.1016/0012-821X(81)90102-3

Alt, J. C. (1995). Seafloor processes in mid-ocean ridge hydrothermal systems. In S. E. Humphris, R. A. Zierenberg, L. S. Mullineaux, & R. E. Thomson (Eds.), *Seafloor hydrothermal systems: Physical, chemical, biological, and geological interactions* (Vol. 91, pp. 85–114). Washington, DC: AGU Monograph.

Alt, J. C., Laverne, C., Coggon, R. M., Teagle, D. A. H., Banerjee, N. R., Morgan, S., et al. (2010). Subsurface structure of a submarine hydrothermal system in ocean crust formed at the East Pacific Rise, ODP/IODP Site 1256. *Geochemistry, Geophysics, Geosystems*, *10*, Q10010. https://doi.org/10.1029/2010GC003144

Alt, J. C., & Teagle, D. A. H. (2003). Hydrothermal alteration of upper oceanic crust formed at a fast-spreading ridge: Mineral, chemical, and isotopic evidence from ODP site 801. *Chemical Geology*, *201*(3-4), 191–211. https://doi.org/10.1016/S0009-2541(03)00201-8

Arnulf, A. F., Singh, S. C., Harding, A. J., Kent, G. M., & Crawford, W. (2011). Strong seismic heterogeneity in layer 2A near hydrothermal vents the mid-Atlantic ridge. *Geophysical Research Letters*, *38*, L08303. https://doi.org/10.1029/2011GL047753

Barker, A. K., Coogan, L. A., Gillis, K. M., & Weis, D. (2008). Strontium isotope constraints on fluid flow in the sheeted dike complex of fast spreading crust: Pervasive fluid flow at Pito Deep. *Geochemistry, Geophysics, Geosystems*, *9*, Q06010. https://doi.org/10.1029/2007GC001901

Barreyre, T., Escartín, J., Garcia, R., Cannat, M., Mittelstaedt, E., & Prados, R. (2012). Structure, temporal evolution, and heat flux estimates from the Lucky Strike deep-sea hydrothermal field derived from seafloor image mosaics: Hydrothermal outflow and image mosaics. *Geochemistry, Geophysics, Geosystems*, *13*, Q04007. https://doi.org/10.1029/2011GC003990

Barreyre, T., & Sohn, R. A. (2016). Poroelastic response of mid-ocean ridge hydrothermal systems to ocean tidal loading: Implications for shallow permeability structure: Shallow upflow zone permeability. *Geophysical Research Letters*, *43*, 1660–1668. https://doi.org/10.1002/2015GL066479

Berndt, M. E., & Seyfried, W. E. Jr. (1990). Boron, bromine, and other trace elements as clues to the fate of chlorine in mid-ocean ridge vent fluids. *Geochimica et Cosmochimica Acta*, *54*(8), 2235–2245. https://doi.org/10.1016/0016-7037(90)90048-P

Berndt, M. E., Seyfried, W. E. Jr., & Beck, W. J. (1988). Hydrothermal alteration processes at mid-ocean ridges: Experimental and theoretical constraints from Ca and Sr exchange reactions and Sr isotopic ratios. *Journal of Geophysical Research*, *93*(B5), 4573–4583. https://doi.org/10.1029/JB093iB05p04573

Besson, P., Degboe, J., Berge, B., Chavagnac, V., Fabre, S., & Berger, G. (2014). Calcium, Na, K and Mg concentrations in seawater by inductively coupled plasma-atomic emission spectrometry: Applications to IAPSO seawater reference material, hydrothermal fluids and synthetic seawater solutions. *Geostandards and Geoanalytical Research*, *38*(3), 355–362. https://doi.org/10.1111/j.1751-908X.2013.00269.x

Bischoff, J. (1991). Densities of liquids and vapors in boiling NaCl-H2O solutions: A PVTX summary from 300° to 500°C. *American Journal of Science*, *291*, 309–338.

Brant, C., Coogan, L. A., Gillis, K. M., Seyfried, W. E. Jr., Pester, N. J., & Spence, J. (2012). Lithium and Li-isotopes in young altered upper oceanic crust from the East Pacific Rise. *Geochimica et Cosmochimica Acta*, *96*, 272–293. https://doi.org/10.1016/j.gca.2012.08.025

Caine, J. S., Bruhn, R. L., & Forster, C. B. (2010). Internal structure, fault rocks, and inferences regarding deformation, fluid flow, and mineralization in the seismogenic stillwater normal fault, Dixie Valley, Nevada. *Journal of Structural Geology*, *32*(11), 1576–1589. https://doi.org/10.1016/j.jsg.2010.03.004

Campbell, A. C., Bowers, T. S., Measures, C. I., Falkner, K. K., Khadem, M., & Edmond, J. (1988). A time series of vent fluid compositions from 21°N, East Pacific Rise (1979, 1981, 1985), and the Guaymas Basin, Gulf of California (1982, 1985). *Journal of Geophysical Research*, *93*(B5), 4537–4549. https://doi.org/10.1029/JB093iB05p04537

Cannat, M., Briais, A., Deplus, C., Escartin, J., Georgen, J., Lin, J., et al. (1999). Mid-Atlantic-Azores hotspot interactions: Along-axis migration of a hotspot-derived event of enhanced magmatism 10 to 4 Ma ago. *Earth and Planetary Science Letters*, *173*(3), 257–269. https://doi.org/10.1016/S0012-821X(99)00234-4

Charlou, J. L., Donval, J. P., Douville, E., Jean-Baptiste, P., Radford-Knoery, J., Fouquet, Y., et al. (2000). Compared geochemical signatures and the evolution of Menez Gwen (37°50′N) and lucky strike (37°17′N) hydrothermal fluids, south of the Azores triple junction on the mid-Atlantic ridge. *Chemical Geology*, *171*(1-2), 49–75. https://doi.org/10.1016/S0009-2541(00)00244-8

Chavagnac, V., Leleu, T., Boulart, C., Barreyre, T., Castillo, A., Menjot, L., et al. (2015). Deep-sea observatory EMSO-Azores (Lucky Strike, 37°17′N MAR): Impact of fluid circulation pathway on chemical hydrothermal fluxes. In *Follow the fluids: Integrating multidisciplinary observations of deep-sea hydrothermal systems II*. San Francisco: AGU Fall Meeting. Abstract OS42A-07

Chavagnac, V., Saleban Ali, H., Jeandel, C., Leleu, T., Destrigneville, C., Castillo, A., et al. (2018). Sulfate minerals control dissolved rare earth element flux and Nd isotope signature of buoyant hydrothermal plume (EMSO-Azores, 37°N mid-Atlantic ridge). *Chemical Geology*. https://doi.org/10.1016/j.chemgeo.2018.09.021

Chen, Y., & Morgan, W. J. (1990). A nonlinear rheology model for mid-ocean ridge Axis topography. *Journal of Geophysical Research*, *95*(B11), 17,583–17,604. https://doi.org/10.1029/JB095iB11p17583

Colaço, A., Blandin, J., Cannat, M., Carval, T., Chavagnac, V., Connelly, D. P., et al. (2011). MoMAR-D: A technological challenge to monitor the dynamics of the Lucky Strike vent ecosystem. *ICES Journal of Marine Science*, *68*(2), 416–424. https://doi.org/10.1093/icesjms/fsq075

Combier, V., Seher, T., Singh, S. C., Crawford, W. C., Cannat, M., Escartín, J., & Dusunur, D. (2015). Three-dimensional geometry of axial magma chamber roof and faults at Lucky Strike volcano on the mid-Atlantic ridge: Magma chamber and faulting at Lucky Strike. *Journal of Geophysical Research: Solid Earth*, *120*, 5379–5400. https://doi.org/10.1002/2015JB012365

Coogan, L. A. (2008). Reconciling temperatures of metamorphism, fluid fluxes, and heat transport in the upper crust at intermediate to fast spreading mid-ocean ridges. *Geochemistry, Geophysics, Geosystems*, *9*, Q02013. https://doi.org/10.1029/2007GC001787

Coumou, D., Driesner, T., Weis, P., & Heinrich, C. A. (2009). Phase separation, brine formation, and salinity variation at black smoker hydrothermal systems. *Journal of Geophysical Research*, *114*, B03212. https://doi.org/10.1029/2008JB005764

Crawford, W. C., Rai, A., Singh, S. C., Cannat, M., Escartin, J., Wang, H., et al. (2013). Hydrothermal seismicity beneath the summit of Lucky Strike volcano, mid-Atlantic ridge. *Earth and Planetary Science Letters*, *373*, 118–128. https://doi.org/10.1016/j.epsl.2013.04.028

Delaney, J. R., Mogk, D. W., & Mottl, M. J. (1987). Quartz-cemented breccias from the mid-Atlantic ridge: Samples of a high-salinity hydrothermal upflow zone. *Journal of Geophysical Research*, *92*, 3767–3787.

Detrick, R. S., Needham, D., & Renard, V. (1995). Gravity-Anomalies and Crustal thickness variations along the Mid-Atlantic Ridge between 33°N and 40°N. *Journal of Geophysical Research*, *100*, 3767–3787. https://doi.org/10.1029/94JB02649

Douville, E., Charlou, J. L., Oelkers, E. H., Bienvenu, P., Jove Colon, C. F., Donval, J. P., et al. (2002). The rainbow vent fluids (36 14′N, MAR): The influence of ultramafic rocks and phase separation on trace metal content in mid-Atlantic ridge hydrothermal fluids. *Chemical Geology*, *184*(1-2), 37–48. https://doi.org/10.1016/S0009-2541(01)00351-5

Driesner, T. (2007). The system $H_2O$–NaCl. Part II: Correlations for molar volume, enthalpy, and isobaric heat capacity from 0 to 1000°C, 1 to 5000 bar, and 0 to 1 XNaCl. *Geochimica et Cosmochimica Acta*, *71*(20), 4902–4919. https://doi.org/10.1016/j.gca.2007.05.026

Driesner, T., & Heinrich, C. A. (2007). The system $H_2O$–NaCl. Part I: Correlation formulae for phase relations in temperature–pressure–composition space from 0 to 1000°C, 0 to 5000 bar, and 0 to 1 XNaCl. *Geochimica et Cosmochimica Acta*, *71*(20), 4880–4901. https://doi.org/10.1016/j.gca.2006.01.033

Elderfield, H., & Schultz, A. (1996). Mid-ocean ridge hydrothermal fluxes and the chemical composition of the ocean. *Annual Review of Earth and Planetary Sciences*, *24*(1), 191–224. https://doi.org/10.1146/annurev.earth.24.1.191

Escartin, J., Barreyre, T., Cannat, M., Garcia, R., Gracias, N., Deschamps, A., et al. (2015). Hydrothermal activity along the slow-spreading Lucky Strike ridge segment (mid-Atlantic ridge): Distribution, heatflux, and geological controls. *Earth and Planetary Science Letters*, *431*, 173–185. https://doi.org/10.1016/j.epsl.2015.09.025

Fontaine, F. J., & Wilcock, W. S. D. (2006). Dynamics and storage of brine in mid-ocean ridge hydrothermal systems. *Journal of Geophysical Research*, *111*, B06102. https://doi.org/10.1029/2005JB003866

Fontaine, F. J., Wilcock, W. S. D., & Butterfield, D. A. (2007). Physical controls on the salinity of mid-ocean ridge hydrothermal vent fluids. *Earth and Planetary Science Letters*, *257*(1-2), 132–145. https://doi.org/10.1016/j.epsl.2007.02.027

Fontaine, F. J., Wilcock, W. S. D., Foustoukos, D. I., & Butterfield, D. A. (2009). A Si-Cl geothermobarometer for the reaction zone of high-temperature, basaltic-hosted mid-ocean ridge hydrothermal systems: Si/Cl-inferred P–T in MOR hydrothermal systems. *Geochemistry, Geophysics, Geosystems*, *10*, Q05009. https://doi.org/10.1029/2009GC002407

Fouquet, Y., Ondréas, H., Charlou, J. L., Donval, J. P., & Radford-Knoery, J. (1995). Atlantic lava lakes and hot vents. *Nature*, *377*(6546), 201. https://doi.org/10.1038/377201a0

Foustoukos, D. I., & Seyfried, W. E. Jr. (2007a). Trace element partitioning between vapor, brine and halite under extreme phase separation conditions. *Geochimica et Cosmochimica Acta*, *71*(8), 2056–2071. https://doi.org/10.1016/j.gca.2007.01.024

Foustoukos, D. I., & Seyfried, W. E. Jr. (2007b). Quartz solubility in the two-phase and critical region of the NaCl–KCl–$H_2O$ system: Implications for submarine hydrothermal vent systems at 9°50′N East Pacific Rise. *Geochimica et Cosmochimica Acta*, *71*(1), 186–201. https://doi.org/10.1016/j.gca.2006.08.038

Foustoukos, D. I., James, R. H., Berndt, M. E., & Seyfried, W. E., (2004). Lithium isotopic systematics of hydrothermal vent fluids at the Main Endeavour Field, Northern Juan de Fuca Ridge. *Chemical Geology*, *212*, 17–26. https://doi.org/10.1016/j.chemgeo.2004.08.003

Goldfarb, M. S., & Delaney, J. R. (1988). Response of two-phase fluids to fracture configurations within submarine hydrothermal systems. *Journal of Geophysical Research*, *93*(B5), 4585–4594.

Hamelin, C., Bezos, A., Dosso, L., Escartin, J., Cannat, M., & Mevel, C. (2013). Atypically depleted upper mantle component revealed by Hf isotopes at Lucky Strike segment. *Chemical Geology*, *341*, 128–139. https://doi.org/10.1016/j.chemgeo.2013.01.013

Heft, K. L., Gillis, K. M., Pollock, M. A., Karson, J. A., & Klein, E. M. (2008). Role of upwelling hydrothermal fluids in the development of alteration patterns at fast spreading ridges: Evidence from the sheeted dike complex at Pito Deep. *Geochemistry, Geophysics, Geosystems*, *9*, Q05O07. https://doi.org/10.1029/2007GC001926

Honnorez, J. (2003). Hydrothermal alteration vs. ocean-floor metamorphism. A comparison between two case histories: The TAG hydrothermal mound (mid-Atlantic ridge) vs. DSDP/ODP hole 504B (equatorial east Pacific). *Comptes Rendus Géoscience*, *335*(10-11), 781–824. https://doi.org/10.1016/j.crte.2003.08.009

Humphris, S. E., Fornari, D. J., Scheirer, D. S., German, C. R., & Parson, L. M. (2002). Geotectonic setting of hydrothermal activity on the summit of Lucky Strike seamount (37°17′N, mid-Atlantic ridge): Geotectonic setting. *Geochemistry, Geophysics, Geosystems*, *3*(8), 1049. https://doi.org/10.1029/2001GC000284

James, R. H., Elderfield, H., & Palmer, M. R. (1995). The chemistry of hydrothermal fluids from the Broken Spur site, 29°N mid-Atlantic ridge. *Geochimica et Cosmochimica Acta*, *59*(4), 651–659. https://doi.org/10.1016/0016-7037(95)00003-I

Jupp, T., & Schultz, A. (2000). A thermodynamic explanation for black smoker temperatures. *Nature*, *403*(6772), 880–883. https://doi.org/10.1038/35002552

Kelley, D. S., & Delaney, J. R. (1987). Two-phase separation and fracturing in mid-ocean ridge gabbros at temperatures greater than 700°C. *Earth and Planetary Science Letters*, *83*(1-4), 53–66. https://doi.org/10.1016/0012-821X(87)90050-1

Kelley, D. S., & Robinson, P. T. (1990). Development of a brine-dominated hydrothermal system at temperatures of 400–500 C in the upper level plutonic sequence, Troodos Ophiolite, Cyprus. *Geochimica et Cosmochimica Acta*, *54*(3), 653–661. https://doi.org/10.1016/0016-7037(90)90361-N

Langmuir, C., Humphris, S. E., Fornari, D. J., Van Dover, C., Von Damm, K. L., Tivey, D., et al. (1997). Hydrothermal vents near a mantle hot spot: The Lucky Strike vent field at 37°N on the mid-Atlantic ridge. *Earth and Planetary Science Letters*, *148*(1-2), 69–91. https://doi.org/10.1016/S0012-821X(97)00027-7

Larson, B. I., Lilley, M. D., & Olson, E. J. (2009). Parameters of subsurface brines and hydrothermal processes 12-15 months after 1999 magmatic event at the Main Endeavor Field as inferred from in situ time series measurements of chloride and temperature. *Journal of Geophysical Research*, *114*, B01207. https://doi.org/10.1029/2008JB005627

Lowell, R. P. (2003). Anhydrite precipitation and the relationship between focused and diffuse flow in seafloor hydrothermal systems. *Journal of Geophysical Research*, *108*(B9), 2424. https://doi.org/10.1029/2002JB002371

Ludwig, K. A., Kelley, D. S., Butterfield, D. A., Nelson, B. K., & Früh-Green, G. (2006). Formation and evolution of carbonate chimneys at the Lost City hydrothermal field. *Geochimica et Cosmochimica Acta*, *70*(14), 3625–3645. https://doi.org/10.1016/j.gca.2006.04.016

Martin, W., Baross, J., Kelley, D., & Russell, M. J. (2008). Hydrothermal vents and the origin of life. *Natural Review of Microbiology*, *6*(11), 805–814. https://doi.org/10.1038/nrmicro1991

Millero, F. J., Feistel, R., Wright, D. G., & McDougall, T. J. (2008). The composition of standard seawater and the definition of the reference-composition salinity scale. *Deep Sea Research*, *55*(1), 50–72. https://doi.org/10.1016/j.dsr.2007.10.001

Miranda, J. M., Luis, J. F., Lourenço, N., & Santos, F. M. (2005). Identification of the magnetization low of the Lucky Strike hydrothermal vent using surface magnetic data: Magnetization low of Lucky Strike. *Journal of Geophysical Research*, *110*, B04013. https://doi.org/10.1029/2004JB003085

Mottl, M. J., Seewald, J. S., Wheat, C. G., Tivey, M. K., Michael, P. J., Proskurowski, G., et al. (2011). Chemistry of hot springs along the Eastern Lau Spreading Center. *Geochimica et Cosmochimica Acta*, *75*(4), 1013–1038. https://doi.org/10.1016/j.gca.2010.12.008

Ondréas, H., Cannat, M., Fouquet, Y., Normand, A., Sarradin, P. M., & Sarrazin, J. (2009). Recent volcanic events and the distribution of hydrothermal venting at the Lucky Strike hydrothermal field, mid-Atlantic ridge: Lucky Strike volcanism and venting. *Geochemistry, Geophysics, Geosystems*, *10*, Q02006. https://doi.org/10.1029/2008GC002171

Palmer, M. R. (1992). Controls over the chloride concentration of submarine hydrothermal vent fluids: Evidence from Sr/Ca and $^{87}Sr/^{86}Sr$ ratios. *Earth and Planetary Science Letters*, *109*(1-2), 37–46. https://doi.org/10.1016/0012-821X(92)90072-4

Person, R., Miranda, J. M., & Puillat, I. (2009). ESONEWS-MoMAR/DA demonstration mission to establish a multidisciplinary observatory at hydrothermal vents on the mid-Atlantic ridge. *Esonews*, *3*, 1–8.

Pester, N. J., Ding, K., & Seyfried, W. E. Jr. (2015). Vapor–liquid partitioning of alkaline earth and transition metals in NaCl-dominated hydrothermal fluids: An experimental study from 360 to 465°C, near-critical to halite saturated conditions. *Geochimica et Cosmochimica Acta*, *168*, 111–132. https://doi.org/10.1016/j.gca.2015.07.028

Pester, N. J., Reeves, E. P., Rough, M. E., Ding, K., Seewald, J. S., & Seyfried, W. E. Jr. (2012). Subseafloor phase equilibria in high-temperature hydrothermal fluids of the Lucky Strike seamount (mid-Atlantic ridge, 37°17′N). *Geochimica et Cosmochimica Acta*, *90*, 303–322. https://doi.org/10.1016/j.gca.2012.05.018

Pester, N. J., Rough, M., Ding, K., & Seyfried, W. E. Jr. (2011). A new Fe/Mn geothermometer for hydrothermal systems: Implications for high-salinity fluids at 13°N on the East Pacific Rise. *Geochimica et Cosmochimica Acta*, *75*(24), 7881–7892. https://doi.org/10.1016/j.gca.2011.08.043

Pokrovski, G. S., Roux, J., & Harrichoury, J. C. (2005). Fluid density control on vapor-liquid partitioning of metals in hydrothermal systems. *Geology*, *33*(8), 657–660. https://doi.org/10.1130/G21475.1

Ravizza, G., Blusztajn, J., Von Damm, K. L., Bray, A. M., Bach, W., & Hart, S. R. (2001). Sr isotope variations in vent fluids from 9° 46′-9° 54′N East Pacific Rise: Evidence of a non-zero-Mg fluid component. *Geochimica et Cosmochimica Acta*, *65*(5), 729–739. https://doi.org/10.1016/S0016-7037(00)00590-1

Reeves, E. P., Seewald, J. S., Saccocia, P., Bach, W., Craddock, P. R., Shanks, W. C., et al. (2011). Geochemistry of hydrothermal fluids from the PACMANUS, northeast Paul and Vienna Woods hydrothermal fields, Manus Basin, Papua New Guinea. *Geochimica et Cosmochimica Acta*, *75*(4), 1088–1123. https://doi.org/10.1016/j.gca.2010.11.008

Resing, J. A., Sedwick, P. N., German, C. R., Jenkins, W. J., Moffett, J. W., Sohst, B. M., & Tagliabue, A. (2015). Basin-scale transport of hydrothermal dissolved metals across the south Pacific Ocean. *Nature*, *523*(7559), 200–203. https://doi.org/10.1038/nature14577

Saccocia, P. J., & Seyfried, W. E. Jr. (1994). The solubility of chlorite solid solutions in 3.2 wt% NaCl fluids from 300–400 °C, 500 bars. *Geochimica et Cosmochimica Acta*, *58*(2), 567–585. https://doi.org/10.1016/0016-7037(94)90489-8

Schmidt, K., Garbe-Schönberg, D., Koschinsky, A., Strauss, H., Jost, C. L., Klevenz, V., & et al. (2011). Fluid elemental and stable isotope composition of the Nibelungen hydrothermal field (8°18′S, mid-Atlantic ridge): Constraints on fluid–rock interaction in heterogeneous lithosphere. *Chemical Geology*, *280*(1-2), 1–18. https://doi.org/10.1016/j.chemgeo.2010.07.008

Schmidt, K., Koschinsky, A., Garbeschonberg, D., Decarvalho, L., & Seifert, R. (2007). Geochemistry of hydrothermal fluids from the ultramafic-hosted Logatchev hydrothermal field, 15°N on the mid-Atlantic ridge: Temporal and spatial investigation. *Chemical Geology*, *242*(1-2), 1–21. https://doi.org/10.1016/j.chemgeo.2007.01.023

Seyfried, W. E. Jr. (2003). Chemistry of hydrothermal vent fluids from the Main Endeavour Field, northern Juan de Fuca Ridge: Geochemical controls in the aftermath of June 1999 seismic events. *Journal of Geophysical Research*, *108*(B9), 2429. https://doi.org/10.1029/2002JB001957

Seyfried, W. E. Jr., Chen, X., & Chan, L. H. (1998). Trace element mobility and lithium isotope exchange during hydrothermal alteration of seafloor weathered basalt: An experimental study at 350 C, 500 bars. *Geochimica et Cosmochimica Acta*, *62*, 949–960.

Singh, S. C., Crawford, W. C., Carton, H., Seher, T., Combier, V., Cannat, M., et al. (2006). Discovery of a magma chamber and faults beneath a mid-Atlantic ridge hydrothermal field. *Nature*, *442*(7106), 1029–1032. https://doi.org/10.1038/nature05105

Steele-MacInnis, M., Han, L., Lowell, R. P., Rimstidt, J. D., & Bodnar, R. J. (2012). The role of fluid phase immiscibility in quartz dissolution and precipitation in sub-seafloor hydrothermal systems. *Earth and Planetary Science Letters*, *321-322*, 139–151. https://doi.org/10.1016/j.epsl.2011.12.037

Stein, C. A., & Stein, S. (1994). Constraints on hydrothermal heat flux through the oceanic lithosphere from global heat flow. *Journal of Geophysical Research*, *99*(B2), 3081–3095. https://doi.org/10.1029/93JB02222

Von Damm, K. L. (1988). Systematics and postulated controls on submarine hydrothermal solution chemistry. *Journal of Geophysical Research*, *93*(B5), 4551–4561. https://doi.org/10.1029/JB093iB05p04551

Von Damm, K. L. (2000). Chemistry of hydrothermal vent fluids from 9–10 N, East Pacific Rise: "Time zero," the immediate post-eruptive period. *Journal of Geophysical Research*, *105*(B5), 11,203–11,222. https://doi.org/10.1029/1999JB900414

Von Damm, K. L., Bischoff, J., & Rosenbauer, R. J. (1991). Quartz solubility in hydrothermal seawater: An experimental study and equation describing quartz solubility for up to 0.5M NaCl solutions. *American Journal of Science*, *291*, 997–1007.

Von Damm, K. L., Bray, A. M., Buttermore, L. G., & Oosting, E. S. (1998). The geochemical controls on vent fluids from the Lucky Strike vent field, mid-Atlantic ridge. *Earth and Planetary Science Letters*, *160*(3-4), 521–536. https://doi.org/10.1016/S0012-821X(98)00108-3

Von Damm, K. L., Lilley, M. D., Shanks, W. C. III, Brockington, M., Bray, A. M., O'Grady, K. M., et al., & the SouEPR Science Party (2003). Extraordinary phase separation and segregation in vent fluids from the southern East Pacific Rise. *Earth and Planetary Science Letters*, *206*(3-4), 365–378. https://doi.org/10.1016/S0012-821X(02)01081-6